Unmanned Aerial Vehicle Relative Navigation in GPS Denied Environments

Jeremy Hardy, Jared Strader, Jason N. Gross, Yu Gu *West Virginia University*
Mark Keck, Joel Douglas, *Systems & Technology Research*
Clark N.Taylor , *Air Force Research Laboratory*

***Abstract*—This paper considers the problem of target handoff between Unmanned Aerial Vehicles (UAVs) in a GPS denied environment, and focuses on the design and evaluation of an estimation strategy for determining the relative pose of the aircraft. The estimation approach presented in this paper has three distinct components that act in concert to achieve the overall objective. First, a novel cooperative control and estimation strategy is used to determine relative pose from IMU and peer-to-peer ranging radio data without any *a priori* knowledge of either aircraft's pose. Next, a relative pose measurement is calculated using extracted features from downward looking cameras on the two UAVs. The computer vision technique first uses an indexing scheme based on a hierarchical statistical model to determine which frames from the two cameras have overlapping coverage, aligns the overlapping frames, and then calculates the relative pose estimate. Finally, a nonlinear Kalman Filter, which has been initialized with the *a priori solution* from the initialization filter is used to estimate relative pose by predicting it through the integration of IMU data of both UAVs with measurement updates from peer-to-peer radio ranging radios, magnetometers and the computer vision estimates.**

***Index Terms*—GPS-Denied Navigation, Relative Inertial Navigation, Relative Pose Computer Vision**

I. Introduction

A. Background and Motivation

ACCURATE relative navigation of groups of UAVs is desirable for many applications involving surveillance, disaster response, formation flight and rendezvous applications, such as aerial re-fueling. Many of these applications require maintaining accurate navigation in environments in which GPS is not always available, either due to malicious GPS jamming and spoofing [1] or due to natural signal blockages from urban canyons, dense foliage, caves, or tunnels. For this work, our specific motivation is to enable target handoff between two UAVs flying in a GPS-denied environment. As such, this paper details and assesses the performance of a relative navigation algorithm that estimates the position and attitude of a UAV with respect to the body-frame of another UAV without the use of GPS.

The goal of this paper is to characterize the sensitivity of the proposed relative pose estimation approach when considering different sensor characteristics, sensor update frequency, initial condition errors and flight dynamics. Through a Monte Carlo analysis, the most important filter design parameters are identified. This will support a candidate design for future hardware implementation and flight testing.

B. Previous Works

Recent work involving relative or cooperative navigation assuming GPS denied environments successfully make use of communicating relative heading and range updates between platforms in order to counteract IMU drift. For example, Sharma and Taylor [2] implement the concept in a simplified two dimensional simulation of several Miniature Air Vehicles (MAVs) and report improvements in pose error compared to IMU only estimation. Additionally, Knuth and Barooah further demonstrate the advantages in [3] by conducting a simulation in which teams of mobile platforms communicate with one another using IMU and relative pose data to estimate pose with respect to an assigned starting point. Knuth and Barooah also confirm this improvement in an experimental setting in which two rovers use optical methods to develop relative pose measurements. Although both of the referenced works above take advantage of information provided by other surrounding platforms to improve pose estimation, both of these examples estimate the pose of all involved vehicles with respect to a common, stationary origin. In contrast, this paper explicitly estimates the pose of one aircraft with respect to the body frame of another aircraft.

The remainder of this paper is organized as follows. Section II details the formulation of algorithm for relative pose estimation developed for this study. Section III outlines the process used in the simulation environment and presents the characteristics of the Monte Carlo setup. Section IV presents the results of the Monte Carlo analysis. Finally, Section V offers conclusions and discusses plan for future continued work on this topic.

II. Algorithm Formulation

Figure 1 shows the assumed sensor payload on the two UAVs simulated for testing in this study, where platform A is assumed to be the UAV currently tracking a target of interest and platform B is having the target handed off to it. Both platforms are assumed to have a downward facing camera, a peer-to-peer ranging radio system, and tri-axial IMU and magnetometer sensors. A communication link for transmitting IMU and magnetometer data and information for the computer vision updates is also assumed. The diagram also displays the assumptions of negligible differences in the magnetic and gravitational fields between platforms, which are leveraged in the filter formulation.

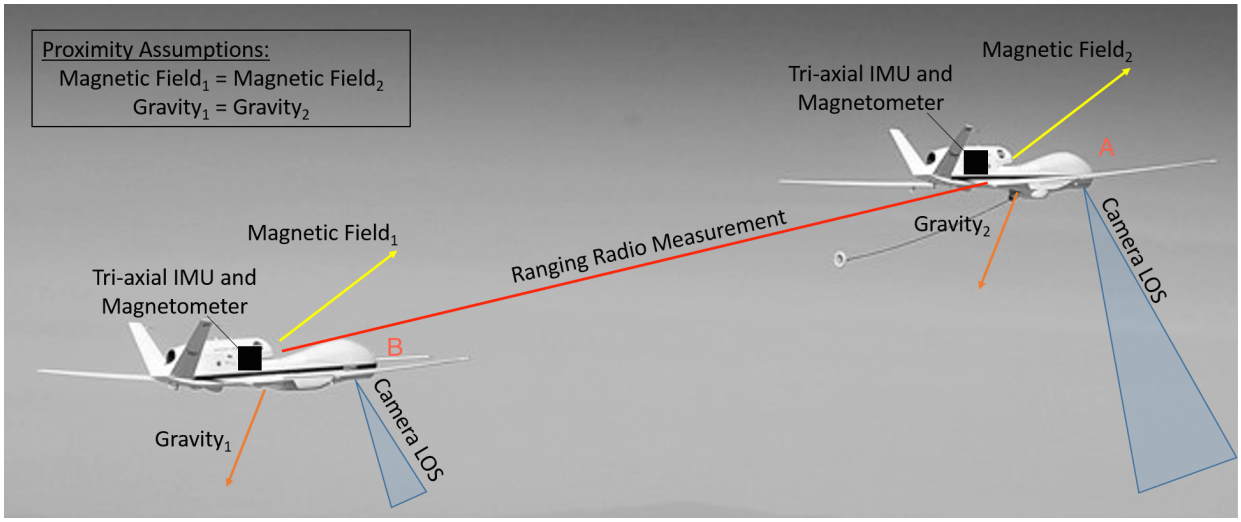

Fig. 1. UAV Platform Payload Diagram and Assumptions

A. *Relative Position Initialization Filter*

For complete details of this filter's formulation and a performance analysis, the reader is pointed to a companion paper [4]. Here, we motivate the high-level concept behind its design.

In this method, there is no prior information needed about the relative pose of each platform. Instead, the motion of each platform is used to construct a graph with the range measurements between platforms and principal component distance traveled over multiple locations. The constructed graph presented in Figure 2 is analogous to a five bar linkage.

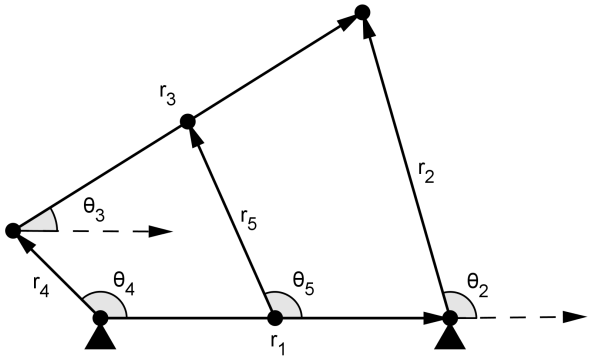

Fig. 2. Trajectories of platforms A and B for three locations where r_1, r_2, r_3, r_4, and r_5 are the link lengths

The distance measurements obtained from the ranging radios and the principal component distance traveled over multiple locations form the links, and the platform position at each location form the joints. To form this linkage, the platforms are required to travel at constant velocities. As listed below, there are four possible scenarios for the solution of this problem while the platforms are traveling at constant velocities. For each of these cases, there is exactly one solution for the relative orientation, but the singularity and the number of solutions of the relative position varies depending on the path of the platforms.

1) If the platforms are traveling along intersecting lines, there are exactly four solutions for the relative position.
2) If the platforms are traveling parallel with different velocities, there are exactly two solutions for the relative position.
3) If the platforms are traveling parallel with equal velocities, there are an infinite number of solutions for the relative position.
4) If the platforms are traveling along the same line in opposite directions, there is exactly one solution for the relative position.

In this problem, only case 1 and case 2 are considered because case 3 and case 4 are easily detectable and are not as likely as case 1 and case 2. Using the constructed linkage, the relative position in polar coordinates can be obtained by solving the loop closure equations of the linkage.

$$\alpha \cos\theta_3 = \beta \tag{1}$$

$$a\tan^2(\theta_2/2) + b\tan(\theta_2/2) + c = 0 \tag{2}$$

In Equation 1, α and β are constant and are a function of the link lengths. In Equation 2, a, b, and c are constant and are a function of the θ_3 and the link lengths. If the system is free of noise, Equation 1 and Equation 2 can simply be solved substituting the appropriate values for the ranging radio measurements and the principal component distance. Since the measurements are noisy, linear least squares is used to solve for the cosine of the relative orientation since this value is constant over any number of time steps. Using the least squares estimate of the cosine of the relative orientation, each of the four possible solutions for the relative position are estimated in polar coordinates using nonlinear least squares to solve Equation 2. Note the value being estimated in Equation 2 is the angular coordinate of the relative position. The radial coordinate is obtained from the ranging radio measurements. Since this formulation is sensitive to noise, the solutions are smoothed using exponential smoothing, then an extended Kalman Filter (EKF) is formed for each solution using INS

for predicting the relative pose and the smoothed angular coordinate for updating the measurements. Once the filters converge, the coordinate frame transformation is calculated for each of the four solutions. At this point, one of the platforms must turn in a different direction and continue traveling at a new constant velocity. Using the estimated coordinate frame transformation, the relative position is propagated during this maneuver using INS. Now, the expected distance between platforms can be calculated using the INS solution. Using the difference between the ranging radio measurement and the expected distance, the likelihood is calculated for each of the four solutions. The solution with the highest likelihood is the solution nearest to the correct solution.

B. Computer Vision Relative Pose Estimation

A commonly used model of image formation is the *pinhole* camera model, which assumes that the model for a camera p can be parameterized using 3 elements: a 3×3 upper triangular intrinsic camera parameter, K^p, a 3×3 rotation matrix, R^p_W, representing a rotation of 3D world points to camera-centered 3D points, and lastly a 3 element vector representing camera p's position in world coordinates, c^p. Given these parameters the full 3×4 perspective projective matrix can be defined by Equation 3.

$$P^p = K^p[R^p_W - R^p_W c^p] \tag{3}$$

Then the transformation projecting a 3D world point y onto 2D image point x^p using the homogeneous coordinate representation can be defined by Equation 4.

$$\tilde{x^p} = P^p \tilde{y} \tag{4}$$

Supposing that two such camera models for cameras A and B were available the relative pose can be directly calculated by subtracting the positions and calculating the rotation matrix between camera A and B.

$$R^B_A = R^B_W (R^A_W)^T \tag{5}$$

With the goal of associating pixels between two images and calculating the relative transformation a three step process is employed. First, the set of images is searched from the two cameras to find corresponding images using a modification of the latent Dirichlet allocation (LDA) [5] coupled to a Hidden Markov Model (HMM). We extract features from the imagery and perform vector quantization in feature space to create a discrete set of "words" (so named because the LDA model was developed for document analysis). The LDA model is a hierarchical statistical model that captures the co-occurrence of features in imagery. Finding corresponding images proceeds by using the statistical model to calculate the maximum likelihood match of the set of features from platform B to the models learned on the images of platform A. The HMM is used to enforce time consistency between observations.

Next, we use a frame-to-frame matching to align the top matching candidate images from the set of corresponding images. A feature-matching approach using the Scale Invariance Feature Transform (SIFT) [6] is used in this study.

Lastly, given the set of correspondences between any two images and the 3×3 intrinsic camera parameter matrix, $\mathbf{K}$, the five-point algorithm [7] can be used to compute an estimate of the essential matrix.

$$E = R^B_A[t^B_A] \tag{6}$$

Where R^B_A represents the relative rotation from platform A's coordinate frame to platform B's and t^B_A represents the relative translation between the two coordinate frames. Thus, a 3D point from platform A's coordinate frame can be transformed into platform B's coordinate frame given the true relative pose.

$$x^B = R^B_A x^A + t^B_A \tag{7}$$

Since E is being recovered from correspondences, only the direction of t^B_A can be computed due to the projective ambiguity.

The relative pose from those correspondences is calculated using the five-point algorithm in a RANdom Sampling and Consensus (RANSAC) [8] loop for robustness.

C. Relative Navigation Filter

The nonlinear estimator used is an unscented Kalman filter (UKF). For details on UKF implementations, the readers are referred to [9] and [10]. The states estimated by the filter are relative position, relative velocity, and relative orientation between platform B and platform A. All of the estimated states are represented in the body frame of platform B.

$$x = \begin{bmatrix} x^B_{AB} \\ y^B_{AB} \\ z^B_{AB} \\ \dot{x}^B_{AB} \\ \dot{y}^B_{AB} \\ \dot{z}^B_{AB} \\ \alpha^B_{AB} \\ \beta^B_{AB} \\ \gamma^B_{AB} \end{bmatrix} = \begin{bmatrix} r^B_{AB} \\ v^B_{AB} \\ \theta^B_{AB} \end{bmatrix} \tag{8}$$

Where x^B_{AB} represents the relative position of platform A with respect to platform B in the x-axis of the body frame of platform B. Similarly, α^B_{AB} represents the relative rotation of platform A around the x-axis of platform B's body axis in order to match orientation with platform B. The nonlinear Kalman filter predicts relative pose using relative INS integration and issues measurement updates provided by computer vision, peer-to-peer ranging radio, and magnetometer sensor data. The filter estimates the relative position and velocity vectors of platform A in the body-frame of platform B, as well as the attitude that represents the transformation from platform A to B, R^B_A.

1) Relative Inertial Navigation: The inertial navigation formulation used in this study was also used by Frosbury and Crassidis in [11], where the authors derived full navigation equations and error-state expressions for relative navigation applications. Frosbury and Crassidis presented this work for its

implications in formation flight control systems and conducted a simulation to prove the validity of the derived equations. In this paper, we slightly deviate from [11] by assuming that there is no gradient in the gravity field between the two platforms.

For predicting relative attitude, a relative quaternion is integrated using data from both platforms IMUs based on state transition relationship derived in [12].

$$q_{AB}^{+} = [\Omega(\omega_B)\Gamma(\omega_A)]q_{AB}^{-} \tag{9}$$

Where $\Omega(\omega_B)$ are $\Gamma(\omega_A)$ are given by:

$$\Omega(\omega_B) = \begin{bmatrix} -[\omega_B\hat{}] & \omega_B \\ -\omega_B^T & 0 \end{bmatrix} \tag{10}$$

and

$$\Gamma(\omega_A) = \begin{bmatrix} [\omega_A\hat{}] & -\omega_A \\ \omega_A^T & 0 \end{bmatrix} \tag{11}$$

Where $\hat{}$ indicates the skew-symmetric matrix of the rotation vector. Using the updated attitude the relative velocity between platforms A and B must take into account the Coriolis acceleration terms due to the rotating body frame of platform B.

$$\begin{aligned} v_{AB}^{B,+} = v_{AB}^{B,-} - (\dot{\omega_B} \times r_{AB}^{B,-})\tau_s - ([\omega_B\hat{}][\omega_B\hat{}]r_{AB}^{B,-})\tau_s - \\ 2(\omega_B \times v_{AB}^{B,-})\tau_s + \Delta v_B - R_A^B \Delta v_A \end{aligned} \tag{12}$$

Where Δv_A and Δv_B are the IMU incremental velocity changes measured in the body-frame of platforms A and B, respectively. It can be noted that there is no modeled acceleration due to gravity present in this equation. It is assumed that the two platforms are close enough to consider the gravity term in the Earth Centered Inertial (ECI) coordinates to be the same for both platforms. Finally, the relative position is predicted using the updated relative velocity estimates as follows:

$$r_{AB}^{B,+} = r_{AB}^{B,-} + (v_{AB}^{B,-})\tau_s \tag{13}$$

The above equations make up the nonlinear state transition functions f of the filter used in this study. The diagonal process noise covariance matrix, Q, is constructed using IMU parameters. Velocity Random Walk (VRW) and Angular Random Walk (ARW) are used to construct the matrix in the same way they would for a single platform INS, with the exception that the matrix is multiplied by a scalar $\sqrt{2}$ to account for the addition of two random error sources (from two separate platforms) instead of one.

2) Measurement Updates: Measurement updates from peer-to-peer ranging radio, magnetometer, and computer vision methods help to minimize the drift present in the relative INS. The observation model for ranging radio measurements is the magnitude of the predicted relative position. The estimated distance, $||r_{AB}^{B,+}||_2$, can be compared to the measured distance provided by ranging radio sensor data. Here we build upon recent work that has used Ultra Wideband (UWB) peer-to-peer radio in a GPS-degraded setting for relative navigation applications for formation flight in [13].

$$||r_{AB}^{B,+}||_2 = \sqrt{(x_{AB}^{B,+})^2 + (y_{AB}^{B,+})^2 + (z_{AB}^{B,+})^2} \tag{14}$$

The magnetometer observation model assumes the same magnetic field vector is acting on each aircraft due to their assumed proximity. Using this assumption the relative attitude between the platforms is used to rotate body axis magnetometer data from platform A into platform B's body frame. Then, the actual measurement from the magnetometer sensors on platform B can be compared to the estimation made from the equation below.

$$M_B = R_A^B M_A \tag{15}$$

The computer vision technique described in Section II-B directly provides relative pose estimates in the form of a unit vector from platform B to platform A, as well as a relative orientation measurement. The measurement error-covariance matrix, R, in the Kalman filter is a diagonal matrix made up of the squares of assigned error values used in the sensor simulation. For magnetometers and ranging radios this is straightforward. The covariance for the computer vision measurements was generated by bounding the empirical statistical error model derived from image data with a Gaussian that included 99% of the errors.

III. Algorithm Sensitivity Analysis

To assess performance sensitivity, a Monte Carlo study was conducted to investigate the effects of varying flight geometry, sensor accuracy, sensor measurement frequency, and initial condition error. As an example, Figure 3 and 4 display the geometry of Flight Path 2. The three flight paths differ in the initial separation between each platform, with Flight Path 1 having the largest separation between aircraft and Flight Path 3 having the smallest. Each of these simulated paths is approximately 8 minutes long, during which the aircraft converge closer to one another to simulate the use of a control system which would navigate platform B to platform A for target hand-off. In reality, this control would be driven by the initialization filter described in [4]. These simulations were conducted in an environment developed at WVU and modified for the purposes of this study, more details of the simulation environment can be found in [14].

The error characteristics of the HG1930-CA50 IMU was used as a baseline for this study and where scaled to error ranges of various grade IMUs [15] and shown in Table I. The baseline Honeywell sensor has a gyroscope bias in-run stability of $1.0\frac{\text{deg}}{hr}$, a accelerometer bias in-run stability of $0.3mg$, a Velocity Random Walk (VRW) of $0.3\frac{fps}{\sqrt{hr}}$ and an Angular Random Walk (ARW) of $0.125\frac{\text{deg}}{\sqrt{hr}}$ in the roll axis and $0.09\frac{\text{deg}}{\sqrt{hr}}$ in the pitch and yaw axes [16]. Additionally, the simulation assumed baseline error characteristics for the ranging radio to be white Gaussian noise $\sigma = 5cm$ and magnetometer measurement errors of white noise Gaussian with $\sigma = 250,000nT$, respectively. Tables II and III show the update rates and error characteristics (Error Scale Factor, ESF) used for the magnetometer, computer vision, and ranging radio

as well as the distribution of initial condition errors used in the Monte Carlo analysis.

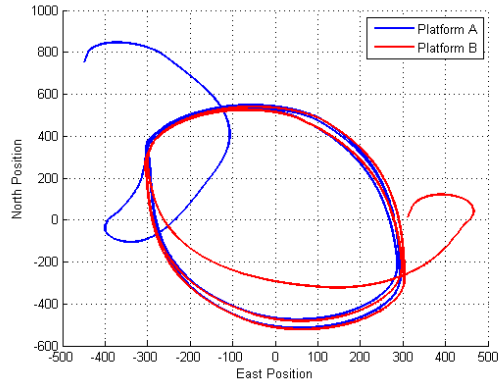

Fig. 3. North v East Representation of Flight Path 2

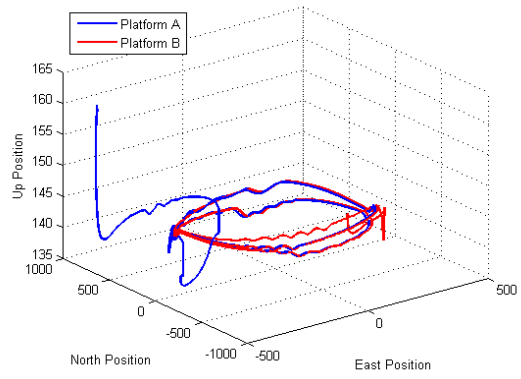

Fig. 4. ENU Representation of Flight Path 2

TABLE I
INERTIAL MEASUREMENT UNIT SCALING FACTORS

IMU Characterization	ESF
Automotive Grade	50
Tactical Grade	1
Intermediate Grade	1/100
Aviation Grade	1/1000

Tables IV - VII show the distribution of different characteristics of the simulation runs included of the 500 Monte Carlo trials that were executed.

IV. RESULTS

A. *Initialization Filter*

The performance analysis of the initialization filter are described in [4]. In this study, we assume an *a prior* initial condition error for the relative pose Kalman filter as shown in Table III.

TABLE II
MAGNETOMETER, RANGING RADIO, AND COMPUTER VISION MONTE CARLO CHARACTERISTICS

Sensor Scaling	Frequency (Hz)	ESF
Magnetometer	100	1-5
Ranging Radio	5, 10, 25, 50, 100	1-5
Computer Vision	1, 2, 5, 10, 25	1

TABLE III
INITIAL CONDITION ERROR DISTRIBUTIONS

Characteristic	Mean	Std. Dev.
Position (m)	0	5
Velocity $(\frac{m}{s})$	0	10
Attitude (deg)	0	2

TABLE IV
IMU QUALITY MONTE CARLO DISTRIBUTION

IMU Quality	# of Runs
IMU 1	126
IMU 2	112
IMU 3	124
IMU 4	138

TABLE V
COMPUTER VISION UPDATE FREQUENCY MONTE CARLO DISTRIBUTION

Computer Vision Frequency (Hz)	# of Runs
1	105
2	95
5	101
10	111
25	88

TABLE VI
RANGING RADIO UPDATE FREQUENCY MONTE CARLO DISTRIBUTION

Ranging Radio Frequency (Hz)	# of Runs
5	89
10	108
25	108
50	108
100	87

TABLE VII
FLIGHT PATH MONTE CARLO DISTRIBUTION

Flight Path	# of Runs
1	164
2	169
3	167

B. Standalone Computer Vision

In order to evaluate computer vision measurements, a two-component Gaussian mixture error model of the five-dimensional relative pose parameter space was estimated. The model was estimated by comparing rotation and translational direction from the computer vision pose estimate on a set of measured data compared to the solution using GPS/INS output. Using 241 test images the best matching images were computed using the LDA-HMM model. Then SIFT matching followed by the five-point algorithm was applied on the query image and the top matching image to estimate the relative pose. The RANSAC estimation process required at least 100 inliers to improve robustness, reducing the number of data points to 159.

The error was computed in both the estimated rotation angles and the difference between the estimated translation vector and the true translation vector in 3 dimensions. An example of the error in rotation angles in shown in Figure 5. Each of the 3 plots shows error in a different angle, computed with respect to the ground-truth axis-angle representation; thus the angles do not directly correspond to roll, pitch, and yaw, but with the error in local coordinates. For the majority of the sequence the error is within a degree, with some earlier parts of the sequence having a larger error. The beginning portion of the sequence is less feature-rich, and therefore, the five-point algorithm is not quite as robust as later in the sequence. Similarly, in Figure 6, the error in translation vector estimate is shown. Note here the clear mode at the origin, with erroneous translation vectors also scattered about space.

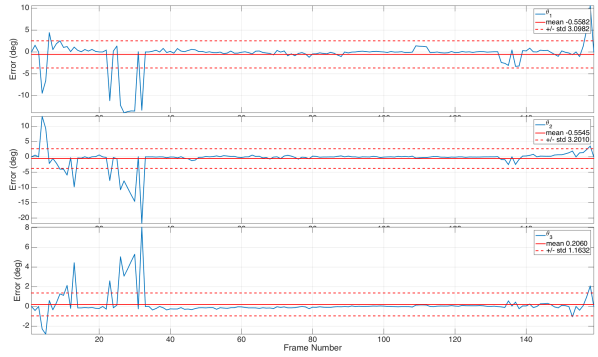

Fig. 5. Error in Rotation Estimate from Five-Point Algorithm

From this data a two-component 6D Gaussian error model for computer vision-based measurements of relative pose was inferred. This model is used in the simulation of computer vision measurements and the variance of the error is used in the relative pose filter.

C. Relative Navigation Filter

For each flight path simulated, the UAVs start far away from one another and eventually converge to a similar trajectory. Over this profile, the most important period for target handoff is after the UAVs have converged to a similar trajectory. During the initial period of the flight when the UAVs are far apart, the estimation error of the filter is relatively poor because errors

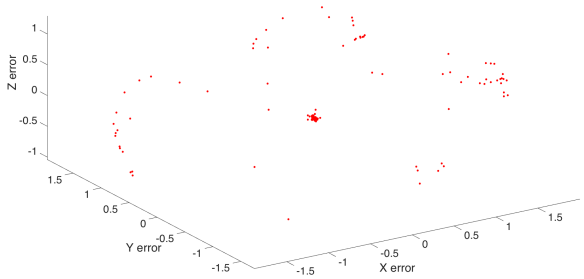

Fig. 6. Error in Translation Vector Estimate from Five-Point Algorithm

in the computer vision system's direction of translation update are projected over a long baseline and the relative dynamics between the UAVs are more exaggerated. As such, our analysis primarily considers the performance over the last 2/3 of each flight. For reference, Figure 7 compares the median error of the 500 Monte Carlo trials over the last 2/3 of each flight where the median is 12 m 3D RSS for position error and 0.5 3D RSS for attitude error.

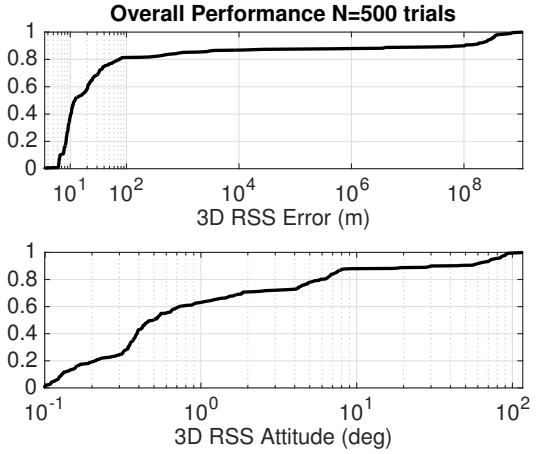

Fig. 7. CDF of Position and Attitude Error from 500 trials (considering last 2/3 of each flight)

All the remaining figures show distributions based upon last 2/3 of each simulated flight separated by run various characteristics. Figures 8 - 14 display Cumulative Distribution Functions (CDFs) for specified simulation characteristics. The position and attitude errors displayed in these plots are the two norm of the Root Mean Square (RMS) error. These plots show the performance of the relative pose filter during the Monte Carlo analysis for a specific simulation characteristic, while all other values of the simulation remain random. For example, Figure 9 displays the results of each filter run sorted by the quality of IMU used during the simulations, while all other Monte Carlo variables are randomized. This allows for the evaluation of the effect IMU quality has on the filter's ability to estimate relative pose.

Figure 8 shows a change in filter accuracy based on flight

geometry, where the closer the starting positions of the aircraft the more accurate the pose estimation than the two with larger initial seperation.

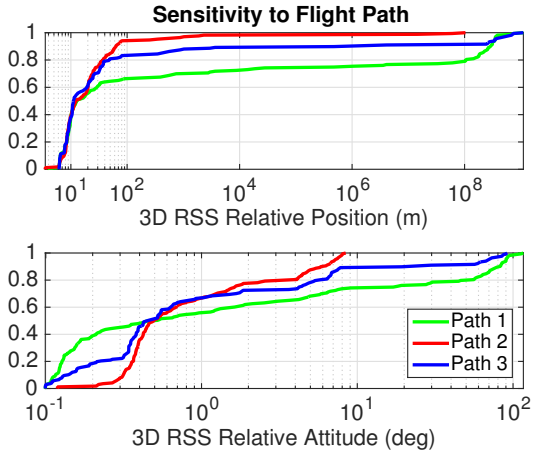

Fig. 8. CDF of Position and Attitude Error from Varying Flight Geometry (considering last 2/3 of each flight)

We believe that this discrepancy is likely attributed to the flights with smaller initial separation containing fewer and less dramatic dynamic maneuvers coupled with the fact that as the separation of the UAVs increases, the errors in the computer-vision based estimates of the direction of translation result in a larger cartesian error.

Figure 9 shows that IMU grade is not very critical for positioning accuracy (i.e. all CDFs are similar), though, as expected, the automotive grade IMUs shows noticeable attitude estimation performance degradation.

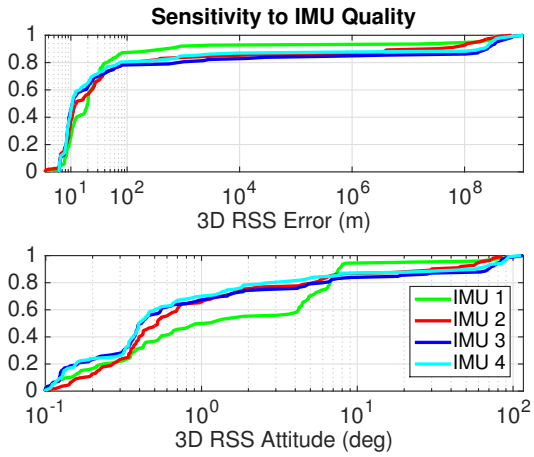

Fig. 9. CDF of Position and Attitude Error from Varying IMU Quality (considering last 2/3 of each flight)

However, the most pronounced differences in estimation accuracy is a result of the computer vision update frequency. Figure 10 displays an obvious trend, in which the filter provides less accurate pose estimations at lower computer vision frequency updates, indicating that these updates are crucial to the filters ability to combat IMU drift.

Interestingly, the remainder of the sensitivities considered as shown in Figures 11 - 14 indicate that there is relatively little

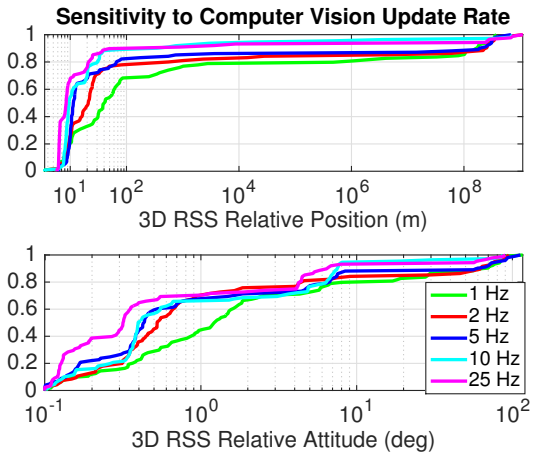

Fig. 10. CDF of Position and Attitude Error from Varying Computer Vision Update Frequency (considering last 2/3 of each flight)

sensitivity on the filter's estimation performance when varying ranging radio update rate, ranging radio and magnetometer error magnitudes, and initial condition errors. That is, each of the CDFs are quite similar for each remaining case.

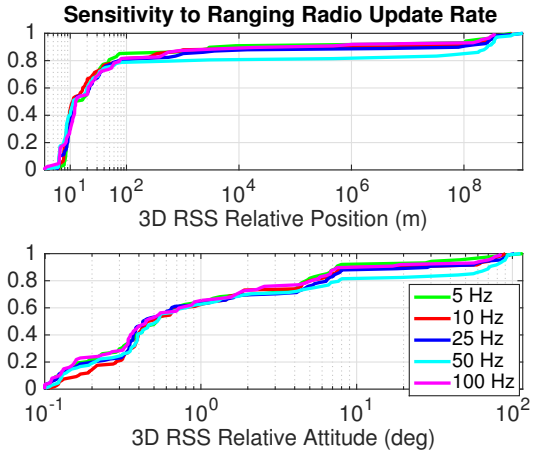

Fig. 11. CDF of Position and Attitude Error from Varying Ranging Radio Update Frequency (considering last 2/3 of each flight)

The fact that the filter formulation produces reasonably accurate position and attitude estimates when considering the ranges of sensor quality and availability tested as shown in Figure 7, is an important determination as we move toward filter and payload design for flight demonstrations. For a baseline design if we only consider trials that use the HG-1930 IMU tactical grade IMU, 5 Hz computer vision updates and assume a favorable flight path, such as flight path 3, the median 3D RSS position error of 13 Monte Carlo trials 21 meters and the median 3D RSS attitude error is 2.7 degrees.

V. Conclusions and Future Work

This study presents a relative pose estimation algorithm and show its sensitivity to flight geometry, sensor characteristics and initial condition errors. The algorithm is a GPS-denied relative navigation filter that primarily consists of an

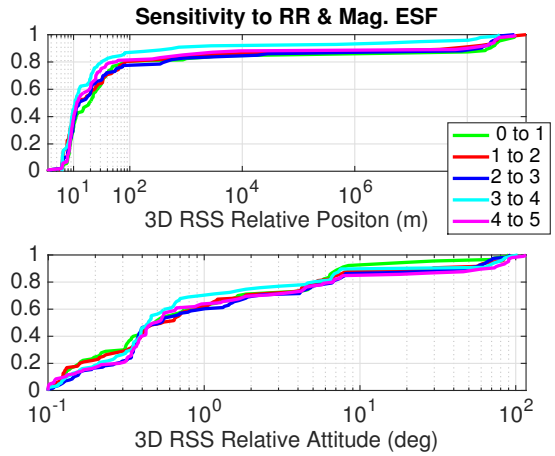

Fig. 12. CDF of Position and Attitude Error from ESF Values of Ranging Radio and Magnetometer Sensors (considering last 2/3 of each flight)

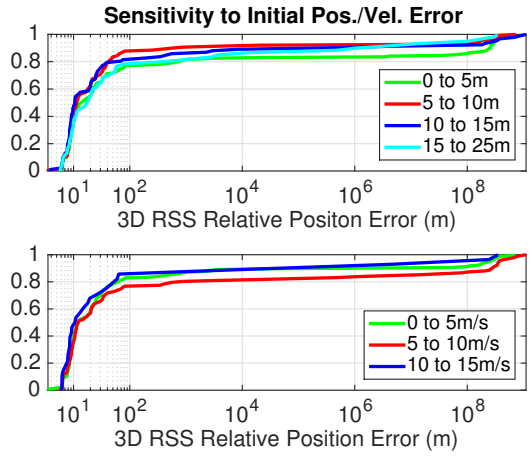

Fig. 13. CDF of Position Error from Initial Condition Errors in Position and Velocity Estimation (considering last 2/3 of each flight)

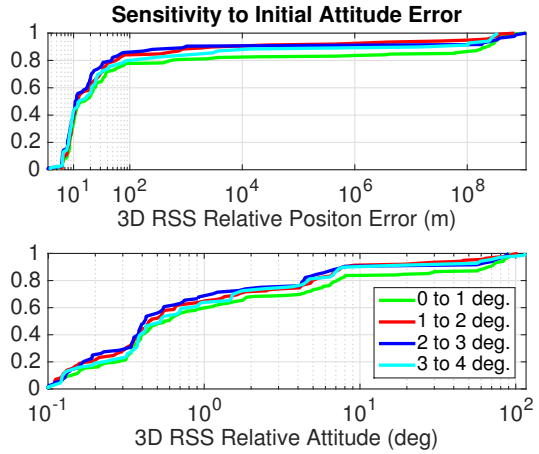

Fig. 14. CDF of Position and Attitude Error from Initial Condition Errors in Attitude Estimation (considering last 2/3 of each flight)

integration of inertial navigation and computer vision. For computer vision updates, a statistical model was used to rapidly determine overlapping content between two sets of imagery such that relative pose can be extracted. Using a set of flight data imagery, a statical error model was developed and used to assess updates of this nature being fused with other sensors. Based on this analysis, it is shown that this algorithm can provide relative pose estimates in a GPS-denied setting with enough accuracy to assist in the problem of platform target handoff. In particular, considering overall

sensitivity to sensor quality and availability, simulated trials were shown to have 10-meter-level position accuracy and 0.5 degree accuracy in a median sense. Our Monte Carlo analysis also shows that the update rate of computer vision relative pose measurements, quality of IMU, and the separation of flight paths have the most prominent impact of performance. Furthermore, the incorporation of magnetometer updates, the quality of ranging radio measurements, and initial condition errors are shown to not have a significant impact on the overall algorithm performance. Future work will include end-to-end system development for experimental testing.

ACKNOWLEDGEMENT

This material is based upon work supported by the United States Air Force under Contract No. FA8650-15-M-1943. Approved for public release, case number 88ABW-2016-0102.

REFERENCES

[1] A. J. Kerns, D. P. Shepard, J. A. Bhatti, and T. E. Humphreys, "Unmanned aircraft capture and control via gps spoofing," *Journal of Field Robotics*, vol. 31, no. 4, pp. 617–636, 2014.

[2] R. Sharma and C. Taylor, "Cooperative navigation of mavs in gps denied areas," in *Multisensor Fusion and Integration for Intelligent Systems*. IEEE, 2008.

[3] J. Knuth and P. Barooah, "Collaborative 3d localization of robots from relative pose measurements using gradient descent on manifolds," in *Robotics and Automation*. IEEE, 2012.

[4] J. Strader, Y. Gu, J. Gross, M. DePetrillo, and J. Hardy, "Cooperative relative localization for uavs with single link range measurements," in *Proceedings of IEEE/ION Position Location and Navigation Symposium*. IEEE/ION, 2016.

[5] D. M. Blei, A. Y. Ng, and M. I. Jordan, "Latent dirichlet allocation," *Jornal of Machine Learning Research*, vol. 3, pp. 993–1022, 2003.

[6] D. Lowe, "Distinctive image features from scale-invariant keypoints," *International Journal of Computer Vision*, vol. 60, no. 2, pp. 91–110, 2004.

[7] H. Stewenius, C. Engels, and D. Nister, "Recent developments on direct relative orientation," *ISPRS Journal of Photogrammetry and Remote Sensing*, vol. 60, no. 4, pp. 284–294, 2006.

[8] M. Fischler and R. Bolles, "Random sample consensus: A paradigm for model fitting with application to image analysis and automated cartography," *Communications of the ACM*, vol. 24, no. 6, pp. 381–395, 1981.

[9] M. Rhudy and Y. Gu, "Understanding nonlinear kalman filters, part ii: An implementation guide," 2013.

[10] D. Simon, *Optimal state estimation: Kalman, H infinity, and nonlinear approaches*. John Wiley & Sons, 2006.

[11] A. M. Fosbury and J. L. Crassidis, "Relative navigation of air vehicles," *Journal of Guidance, Control, and Dynamics*, vol. 31, no. 4, pp. 284–834, 2008.

[12] R. A. Mayo, "Relative quaternion state transition relation," *Journal of Guidance, Control, and Dynamics*, vol. 2, no. 1, pp. 44–48, 1979.

[13] J. N. Gross, Y. Gu, and M. B. Rhudy, "Robust uav relative navigation with dgps, ins, and peer-to-peer radio ranging," *Automation Science and Engineering, IEEE Transactions*, vol. 12, no. 3, pp. 935–944, 2015.

[14] R. Watson, V. Sivaneri, and J. Gross, "Performance Characterization of Tightly-Coupled GNSS Precise Point Positioning Inertial Navigation within a Simulation Environment," in *2016 AIAA Guidance Navigation and Control Conference*. AIAA, 2016.

[15] P. D. Groves, *Principles of GNSS, inertial, and multisensor integrated navigation systems*. Artech House, 2013.

[16] "Hg1930 datasheet," https://aerospace.honeywell.com/products/communication-nav-and-surveillance/inertial-navigation/inertial-measurement-units/hg1930, 2015.